Incorporating Rare-earth Tb3+ into Cs2AgInCl6:Bi Nanocrystals toward Tunable Photoluminescence

Journal:	*Journal of the American Chemical Society*
Manuscript ID	ja-2020-02080c
Manuscript Type:	Article
Date Submitted by the Author:	21-Feb-2020
Complete List of Authors:	Liu, Ying; University of Science and Technology Beijing Rong, Ximing; Shenzhen University, College of Physics and Optoelectronic Engineering Li, Mingze; University of Science and Technology Beijing Molokeev, Maxim; Institut fiziki imeni Kirenskogo SO RAN, Zhao, Jing; University of Science and Technology Beijing, School of Materials Sciences and Engineering Xia, Zhiguo; South China University of Technology, State Key Laboratory of Luminescent Materials and Devices and School of Materials Science and Engineering

SCHOLARONE™
Manuscripts

Incorporating Rare-earth Tb^{3+} into $Cs_2AgInCl_6$:Bi Nanocrystals toward Tunable Photoluminescence

Ying Liu[‡,†], Ximing Rong[‡,§] Mingze Li[†], Maxim S. Molokeev[#,Δ,⊥], Jing Zhao[†], Zhiguo Xia[†,*]

[†]The Beijing Municipal Key Laboratory of New Energy Materials and Technologies, School of Materials Sciences and Engineering, University of Science and Technology Beijing, Beijing 100083, China

[§]Shenzhen Key Laboratory of Special Functional Materials, Shenzhen Engineering Laboratory for Advanced Technology of Ceramics, Guangdong Research Center for Interfacial Engineering of Functional Materials, College of Materials Science and Engineering, Shenzhen University, Shenzhen 518060, China

[#]Laboratory of Crystal Physics, Kirensky Institute of Physics, Federal Research Center KSC SB RAS, Krasnoyarsk 660036, Russia

[Δ]Siberian Federal University, Krasnoyarsk, 660041, Russia

[⊥]Department of Physics, Far Eastern State Transport University, Khabarovsk, 680021, Russia

[*]State Key Laboratory of Luminescent Materials and Devices and Guangdong Provincial Key Laboratory of Fiber Laser Materials and Applied Techniques, South China University of Technology, Guangzhou 510641, China

ABSTRACT: Lead-free halide perovskite nanocrystals (NCs) are reported as promising candidates for emerging optoelectronic applications but are limited by their monotonous photoluminescence. Herein, we establish relationships between rare earth ions doping and intrinsic emission of double perovskite $Cs_2AgInCl_6$ NCs to impart and tune the optical performances in the visible light region. Tb^{3+} ions were incorporated into $Cs_2AgInCl_6$ NCs and occupied In^{3+} sites verified by both experimental analyses and first-principles calculations. Trace amount of Bi doping endowed the characteristic emission ($^5D_4 \rightarrow {}^7F_{6-3}$) of Tb^{3+} ions with new excitation peak at 368 nm rather than single characteristic excitation at 290 nm of Tb^{3+}. By controlling Tb^{3+} ions concentration, the emission colors of $Cs_2AgInCl_6$:Bi,Tb NCs could be continuously tuned from green to orange, due to the efficient energy transfer channel from self-trapped excitons to Tb^{3+} ions. Our study provides the underlying insights to guide the design optimization of lead-free perovskite NCs and to expand their luminescence applications.

INTRODUCTION

Lead-free halide perovskite nanocrystals (NCs) have attracted intense research efforts recently as possible lead-halide perovskite NCs alternatives to address the ambient instability and lead toxicity issues for the realization of business development.[1-3] Several classes of related materials that replace lead with other elements have been explored.[4] Isovalent substitution of Pb^{2+} with less-toxic Sn^{2+} or Ge^{2+} is a straightforward method. Unfortunately, the resulting compounds $CsBX_3$ (B = Sn^{2+} and Ge^{2+}) exhibit poorer stabilities than lead-halide perovskites ascribed to the easy oxidations of Sn^{2+} and Ge^{2+} to their corresponding 4+ states.[5] Another important alternative approach to replace two Pb^{2+} ions with one monovalent (M') and one trivalent (M'') cation to form the M' and M'' octahedra, obtaining a $A_2M'M''X_6$ three dimensional (3D) double perovskite structure. Theoretically, in the generic chemical formula $A_2M'M''X_6$, M' could be Ag^+, Na^+, Cu^+ and M'' could be Bi^{3+}, Sb^{3+}, In^{3+} to form many possible compositions.[6,7] Experimentally, Cs_2AgBiX_6, $Cs_2AgInCl_6$, $Cs_2AgSbCl_6$, $Cs_2NaBiCl_6$ and their alloys have been synthesized as colloidal NCs.[8-11] However, most air-stable double perovskite NCs possess either large bandgaps or forbidden optical transition,[12-14] leaving the challenges in realizing optoelectronic applications and thus motivating researchers to develop strategies to improve the optoelectronic properties.[15,16]

Lanthanide (rare earth) ions incorporation or doping is considered as a promising approach to imparting and tailoring the optical and optoelectronic performances of inorganic materials over the visible and near infrared region. The lanthanide ions (Ln^{3+}) usually exhibit unique emissions with sharp spectral linewidths compared with transition metal ions whose emissions are relatively broadband. Nevertheless, it is noteworthy that Ln^{3+} ions prefer locating in the sites with coordination environment CN ≥ 6 and lead-free double perovskites and lead halide perovskites exactly possess the octahedral coordination (CN = 6) for B-site cation and M''-site cation, respectively, being the ideal hosts for lanthanide ion incorporation.[17] For lead-halide perovskite NCs, different lanthanide ions have been successfully doped into the lattice for imparting optical functionality or improving the stability of NCs.[18-23]

However, to the best of our knowledge, only several successful examples of Ln^{3+} ions doping into the lead-free perovskite NCs were reported so far, mostly in the near infrared region. For example, Yb^{3+} or Er^{3+} ions doping into $Cs_2AgInCl_6$ NCs was explored by Kim's and Nag's group;[24,25] Chen et al. doped Yb^{3+} and Mn^{2+} ions into Cs_2AgBiX_6 NCs;[26] Tang's group doped Ho^{3+} ions into $Cs_2AgNaInCl_6$ NCs;[27] Song et al. reported Eu^{3+}-doped $Cs_3Bi_2Br_9$ quantum dots for Cu^{2+} detection.[28] Inspired by the studies described above, it is valuable to unveil new Ln^{3+} ions doping effects on lead-free double perovskite NCs and impart the optical properties in the visible range.

Herein, we successfully incorporated Tb^{3+} ions into lead-free double perovskite $Cs_2AgInCl_6$ NCs, simultaneously preserving the consistent crystal structure and uniform cubic morphology, to impart and tune the photoluminescence performances. Accordingly, the Tb^{3+} ions site occupation was verified from experimental analyses and first-principles calculations. More importantly, Bi^{3+} ions doping in $Cs_2AgInCl_6$ NCs adjusted the excitation of Tb^{3+} ions emission to 368 nm and variation of Tb^{3+} ions doping concentration achieved tunable emission colors from green to orange. Moreover, we explored the emission mechanism and further proposed the efficient energy transfer channel with 368 nm excitation from self-trapped excitons (STEs) to Tb^{3+} ions in $Cs_2AgInCl_6$:Bi,Tb NCs. Our study provides insights to dope Ln^{3+} ions into the lead-free double perovskite NCs to generate multiple emissions and to expand their potential as optoelectronic materials.

EXPERIMENTAL SECTION

Materials. Silver nitrate ($AgNO_3$, analytical pure), indium chloride ($InCl_3$, 99.99%), terbium(III) nitrate pentahydrate ($Tb(NO_3)_3 \cdot 5H_2O$, 99.9%), bismuth chloride ($BiCl_3$, 99.99%), cesium carbonate (Cs_2CO_3, 99.9%), octadecene (ODE, >90%), oleylamine (OLA, 80-90%), oleic acid (OA, analytical pure), hydrochloric acid (HCl, analytical pure), hexane (C_6H_{14}, ≥98%), ethyl acetate ($C_4H_8O_2$, analytical pure). $AgNO_3$ and HCl were purchased from Beijing Chemical Works, China. Ethyl acetate was purchased from Sinopharm. All chemicals were used as received directly.

Synthesis of Cs-Oleate. Cs_2CO_3 (0.814 g) was added into a 50 mL three-necked flask with ODE (10 mL) and OA (2.5 mL), degassed under vacuum at 120 °C for 1 h and filled with N_2. To completely dissolve Cs_2CO_3, the mixture was subsequently heated up to 150 °C.

Synthesis of $Cs_2AgInCl_6$ and $Cs_2AgInCl_6$:1%Bi nanocrystals (NCs). $AgNO_3$ (0.36 mmol), $InCl_3$ (0.36 mmol), $BiCl_3$ (0.0036 mmol), $Tb(NO_3)_3 \cdot 5H_2O$ (Tb/In precursors ratio of 0, 0.02, 0.05, 0.1, 0.3, 0.5, 0.8), 14 mL of ODE, 1 mL of OA, 1 mL of OLA and 0.28 mL of HCl were loaded into a 50 mL three-necked flask and degassed under vacuum for 1 h at 120 °C, and then the temperature was raised to 260 °C under N_2 and hot (150 °C) Cs-oleate solution (0.8 mL) was quickly injected. The system was quenched by an ice-water bath after five seconds. The crude solution was centrifuged at 8000 rpm for 4 min and then the precipitates were resuspended in hexane. Another centrifugation process

(4 min at 5000 rpm) was performed and the supernatant was precipitated with ethyl acetate. The solution was centrifuged again at 10000 rpm for 4 min, obtaining the final NCs by discarding the supernatant.

Characterization. X-ray diffraction (XRD) measurements were carried out on an Aeris X-ray diffractometer (PANalytical Corporation, Netherlands) equipped with a 50000 mW Cu Kα radiation operating at 40 kV and 15 mA under ambient conditions. Samples for XRD analysis were prepared by dropping concentrated nanocrystals hexane solutions onto the silicon substrates. Transmission electron microscopy (TEM) images and energy-dispersive X-ray spectroscopy (EDS) analysis were obtained by using a JEM-2010 microscope working at 120 kV. TEM samples were prepared by drop casting dilute dispersion of samples onto an ultrathin carbon film coated Cu grids. Absorption spectra in the ultraviolet–visible (UV–vis) region were collected by using a Hitachi UH4150 UV–vis–near IR spectrophotometer. Photoluminescence (PL) spectra, photoluminescence excitation (PLE) spectra and PL decay spectra of NCs were acquired on a FLS920 fluorescence spectrometer (Edinburgh Instruments Ltd., U.K.) Instruments equipped with the Xe900 lamp, nF920 flash lamp and the PMT detector. Elemental analysis was using inductively coupled plasma mass spectroscopy (ICP-MS) by the wet digestion method. The extended X-ray absorption fine structure (EXAFS) spectra of the Tb L_3-edge were recorded on the 1W1B beam line in the transmission mode at Beijing Synchrotron Radiation Facility. The NC powders were dispersed on a single-faced adhesive tape (Scotch). The PL quantum yields were obtained on the Hamamatsu absolute PL quantum yield spectrometer C11347 Quantaurus_QY.

COMPUTATIONAL METHODOLOGY

First-principles Calculations. In this work, all first-principles calculations were performed based on the density functional theory (DFT), as implemented in the Vienna ab initio simulation package (VASP) code.[29,30] The projector augmented wave (PAW) potential method[31] was used to describe the interactions between ions and electrons, and the exchange–correlation interactions between electrons were treated within the generalized gradient approximation (GGA–PBE).[32] The plane wave cut-off energy of 520 eV was used for all structural optimizations and electronic calculations. The K-point meshes were generated according to the Monkhorst–Pack scheme[33] for the Brillouin zones, as Γ-centered with a k-grid density of $0.02 \times 2\pi$ Å^{-1} for ionic interactions and electronic SCF interactions. The convergence criterion for the energy in electronic SCF iterations and the force in ionic step iterations were set to 1.0×10^{-6} eV and 1.0×10^{-2} eV Å^{-1}, respectively.

Dopant Structures. A $2 \times 2 \times 2$ super cell structure (80 atoms) was set up for the Tb^{3+}-doped $Cs_2AgInCl_6$ system, which has already been discussed to be enough for the defect simulation of double perovskite structures in our previous work.[34] For different Tb^{3+} ions doping concentrations, certain amount of In atoms in

$Cs_2AgInCl_6$ super cell were replaced by Tb atoms to achieve the Tb^{3+} ions concentration of substitution doping. For each doping concentration, all possible substitution site of In atoms were considered and all substitution doping structures were fully relaxed. The dopant structures with the lowest total energy were chosen to be the desired structure for certain concentration, and all total energies, volumes, optical and electrical properties of Tb^{3+}-doped $Cs_2AgInCl_6$ with different concentrations were calculated based on the desired structures.

RESULTS AND DISCUSSION

All samples were synthesized via high temperature hot injection method reported in our previous work.[35] To clarify whether the rare earth Tb^{3+} ion is doped into the $Cs_2AgInCl_6$:Bi NCs, XRD patterns of the as-prepared $Cs_2AgInCl_6$:Bi,xTb (x = 0, 9.1%, 17.5%, 20.6%) NCs were firstly analyzed as shown in Figure 1. All the NCs possessed the same cubic phase with no impurity detected and slight shifts of the diffraction peak of (022) plane toward smaller angle were observed for the doped samples (Figure 1a). The amounts of Tb^{3+} ions included in the nanocrystals were ascertained by the inductively coupled plasma (ICP) measurement (Table S1). Figure 1b, c further present Rietveld refinement of the XRD patterns of undoped and 20.6 mol% Tb^{3+}-doped $Cs_2AgInCl_6$:Bi nanocrystals. All the peaks were indexed by orthorhombic cell (Fm-$3m$) with parameters close to the bulk $Cs_2AgInCl_6$.[36] Therefore, this structure was taken as the starting model for Rietveld refinement performed using TOPAS 4.2. Refinements were stable and gave low R-factors (Table S2, Figure 1b, c). Coordinates of atoms and main bond lengths were present in Table S3 and Table S4, respectively. Corresponding to the peak shift in Figure 1a, the cell volume $V(x)$ increased with Tb^{3+} ions doping concentrations x as shown in Figure 1d. Considering that the ionic radii $r(Tb^{3+}$, CN = 6) = 0.923 Å is smaller than $r(Cs^+$, CN = 12) = 1.88 Å and $r(Ag^+$, CN = 6) = 1.15 Å, Tb^{3+} ions should not locate in Cs and Ag sites. Only the ionic radii $r(In^{3+}$, CN = 6) = 0.8 Å is smaller than that of Tb^{3+} ions, which verifies that the partial Tb^{3+} ions are incorporated into the lattice of $Cs_2AgInCl_6$ NCs and substitute partial In^{3+} ions.

To further clarify the occupied crystallographic sites of Tb^{3+} ions in the $Cs_2AgInCl_6$ lattice, Tb L_3-edge EXAFS measurement and analysis for the $Cs_2AgInCl_6$:Bi, 20.6%Tb NCs were conducted and demonstrated in Figure 1e, f. The obtained EXAFS data was processed in Athena (version 0.9.25) for background, pre-edge line and post-edge line calibrations. Then corresponding Fourier transform (FT) fitting was carried out in Artemis (version 0.9.25). The k^2 weighting, k-range of 3 - 12 Å^{-1} and R range of 1 – 3 Å were used for the fitting. The model of Tb^{3+} ions at In^{3+} sites in $Cs_2AgInCl_6$ was used to calculate the simulated scattering paths. The four parameters: coordination number (CN), bond length (R), Debye-Waller factor (σ^2) and
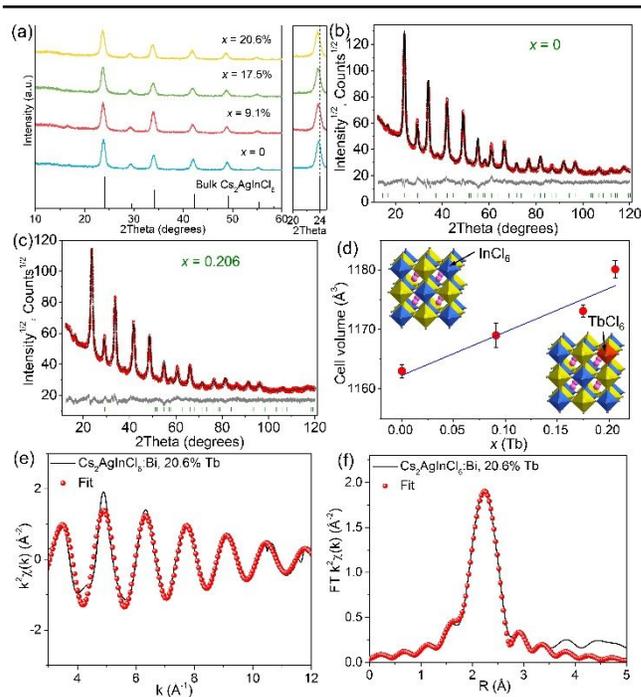
Figure 1. (a) XRD patterns of undoped and Tb^{3+}-doped $Cs_2AgInCl_6$:Bi NCs with different Tb^{3+} ions doping concentrations x (left) and magnified XRD patterns in the range of 20~25 $^\circ$ (right). (b, c) Rietveld refinement of XRD patterns for $Cs_2AgInCl_6$:Bi and $Cs_2AgInCl_6$:Bi,20.6%Tb, respectively. (d) Variation of cell volume as a function of doping concentration x. Insets show the schematic of corresponding crystal structure with Tb^{3+} ions doping. (e) k^2-weighted Tb L_3-edge EXAFS spectrum and (f) corresponding Fourier transform of $Cs_2AgInCl_6$:Bi, 20.6%Tb NCs fitting as a function of R.

E_o shift (ΔE_o) were fitted without fixed, constrained, or correlated. It can be seen that in Figure 1e, f the spectra were fitted well, with CN = 5.6±0.4, ΔE_o = 4.6±0.6 eV, σ^2 = 0.0051±0.0006 Å^2, and R factor = 0.003. As exhibited in Figure 1f, the position of the peak in R space (viz., the interatomic distance from the absorbing atom Tb to the nearest atom Cl) is ca. 2.24 Å, shorter than the bond length of In-Cl (2.56 Å) while much shorter than that of Ag-Cl (2.72 Å) and Cs-Cl (3.74 Å) obtained from the refinement results (Table S4) of $Cs_2AgInCl_6$:Bi, 20.6%Tb NCs. In the FT, the relative decrease in the peak position compared with the actual interatomic distance could attribute to the photoelectron phase shift.[37] In conclusion, all these results support that the doped Tb^{3+} ions occupied In^{3+} sites.

XPS analyses were also performed to confirm the presence of Tb in the $Cs_2AgInCl_6$:Bi,Tb NCs (Figure S1). The survey XPS spectrum (Figure S1a) showed that both undoped and Tb^{3+} ions doped NCs contained Cs, Ag, In, Cl elements, however, only small amount of Tb can be found in Tb^{3+}-doped NCs. Figure S1b exhibited the two peaks of Tb 3d signals at 1242 and 1277 eV in the 20.6 mol% Tb^{3+}-doped sample readily proving the existence of Tb^{3+} ions in the $Cs_2AgInCl_6$:Bi NCs. Furthermore, comparing the high resolution XPS spectra of In 3d and Ag 3d for Tb^{3+}-doped and undoped NCs (Figure S1c, d), a slight shift to higher binding energy for In^{3+} $3d_{3/2}$ and In^{3+} $3d_{5/2}$ but little variations for Ag^{3+} 3d appeared. The

slight shift could attribute to the lattice expansion after the successful incorporation of Tb^{3+} ions, further confirming the conclusion above that Tb^{3+} ions occupy In^{3+} sites rather than Ag^+ sites.[22] TEM images shown in Figure 2a, c, e, g demonstrated the microstructure of as-prepared undoped and Tb^{3+}-doped $Cs_2AgInCl_6$:Bi NCs. It can be seen that the NCs have similar cubic morphology with the high crystallinity and uniformity. 'Dark dots' attached on the NCs could be Ag^o NCs that have been discussed in previous studies.[10,35] The selected area electron diffraction (SAED) patterns of corresponding NCs shown in Figure 2b, d, f, h revealed the presence of (022) and (004) planes of cubic phase, confirming the formation of the consistent perovskite structure. Moreover, as presented in insets of Figure 2a, c, e, g, the lattice constants increased from 0.37 to 0.39 nm with the increase in Tb^{3+} ions doping concentration, further verifying the lattice expansion consistent with the XRD results above.
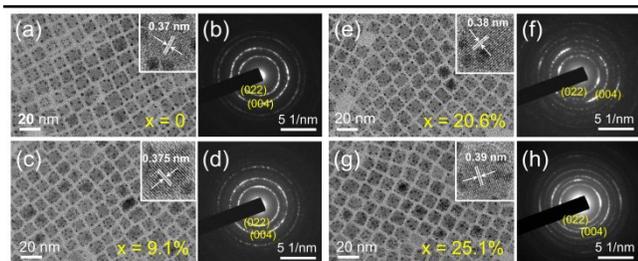
Figure 2. (a, c, e, g) TEM and HRTEM images of $Cs_2AgInCl_6$:Bi,xTb (x = 0, 9.1%, 20.6%, 25.1%) NCs, respectively. (b, d, f, h) Corresponding SAED patterns of Tb^{3+} ions doped $Cs_2AgInCl_6$:Bi NCs.

Next, we performed first-principles calculations for simulating the difficulty in defect formation and the stabilities of the defect systems of Tb^{3+} ions incorporated into $Cs_2AgInCl_6$ lattice. Figure 3a showed the relaxed structures of six possible dopant conditions (named A to F) of Tb^{3+}-doped $Cs_2AgInCl_6$, where A ~ C represented interstitial doping of Tb located previously between nearest Cs-Cs, Cs-Ag and Cs-In atoms, while D ~ F represented substitution doping of Tb at Cs, Ag and In site, respectively. The interstitial formation energies (for A ~ C) were calculated by formula:

$$E_{for} = E_{tot}(Cs_2AgInCl_6 + Tb) - E_{tot}(Cs_2AgInCl_6) - \mu_{Tb}$$

For substitution situations, the substitution formation energies (for D ~ F) were calculated by formula:

$$E_{for} = E_{tot}(Cs_2AgInCl_6 + Tb) - E_{tot}(Cs_2AgInCl_6) + \mu_X - \mu_{Tb}$$

where $E_{tot}(Cs_2AgInCl_6 + Tb)$ and $E_{tot}(Cs_2AgInCl_6)$ represent the total energy of Tb-doped $Cs_2AgInCl_6$ system and undoped $Cs_2AgInCl_6$ crystal, respectively. μ_X (X = Cs, Ag or In) and μ_{Tb} is the chemical potential of the substitution atom (Cs, Ag or In) and Tb atom calculated as the corresponding crystal energy per atom. All the formation energies for different dopant conditions are graphically represented in Figure 3b. Condition D (Cs-poor condition) has positive formation energies compared with other doping
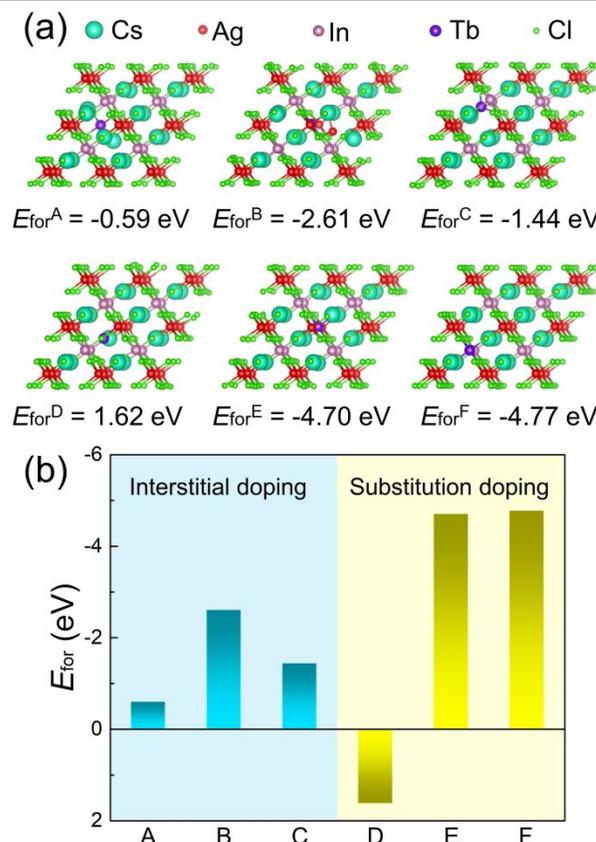
Figure 3. (a) Relaxed structures of possible doping conditions of $Cs_2AgInCl_6$ with Tb^{3+} dopant; (b) Formation energies for different doping conditions. Condition A ~ C: interstitial doping of Tb located previously between nearest Cs-Cs, Cs-Ag and Cs-In atoms, respectively; condition D ~ F: substitution doping of Tb at Cs, Ag and In site, respectively.

conditions with negative formation energies, indicating an inappropriate solubility of substitution doping of Tb in Cs-poor condition. For other substitution doping conditions, the formation energies are lower than those of interstitial doping conditions, and In-poor conditions (Condition F) has the lowest E_{for} of -4.77 eV, indicating that Ag-poor and In-poor environments are more favorable, and Tb substitution at In site was expected to be more easily realized and more feasibly synthesized than Ag site and other interstitial doping in experiments. Besides, the doping of Tb^{3+} ions at In^{3+} ions site could be more favorable as an isoelectronic doping rather than other charged doping site or interstitial doping. In combination of the EXAFS, XPS analyses and the ionic radii comparisons discussed previously, the substitution of Tb atoms at In^{3+} site could be the main occupation for Tb^{3+} ions involved $Cs_2AgInCl_6$.

The dopant structures with different Tb^{3+} ions doping concentrations were established and fully relaxed with details introduced in the computational method section. For the dopant $Cs_2AgInCl_6$, the calculated structural volume increased 0.77% and 1.62% for Tb^{3+} ions doping concentration of 12.5% and 25%, respectively, which is in consistent with the variation tendency of experimental measurement (see Figure 1d). The calculated absorption coefficients for $Cs_2AgInCl_6$ with different doping concentrations were shown in Figure S2a, as the band

edge showed obvious blue shift as the Tb^{3+} ions doping concentration increased, causing enhancement of the optical bandgap. Such bandgap expansion could also be confirmed in the calculated total density of state (TDOS) shown in Figure S2b, where the conduction band minimum (CBM) moved towards higher energy level when Tb^{3+} ions concentration increased. This could be contributed to the Tb involvement in the $Cs_2AgInCl_6$. The Tb^{3+}-doped $Cs_2AgInCl_6$ could be understood as a solid solution $Cs_2AgIn_{1-x}Tb_xCl_6$ which could be decomposes to two stable double perovskite: $Cs_2AgInCl_6$ and $Cs_2AgTbCl_6$ (both Fm-$3m$). As the PBE bandgap of $Cs_2AgTbCl_6$ (3.63 eV) is larger than that of $Cs_2AgInCl_6$ (1.03 eV), the bandgap for the Tb^{3+} ions incorporated $Cs_2AgInCl_6$ could be inevitably enlarged when the Tb^{3+} ions concentration increased. Such bandgap variation has already been observed in solid solution perovskite systems with both cation[16] and anion[38] transmutation. The partial density of state (PDOS) for undoped, 12.5% Tb^{3+}-doped and 25% Tb^{3+}-doped $Cs_2AgInCl_6$ are represented in Figure S2c-e. For Tb^{3+}-doped $Cs_2AgInCl_6$, the upper valence band and valence band maximum (VBM) are mainly contributed by Cl 3p and Ag 3d orbitals analogous to $Cs_2AgInCl_6$, while the CBM state is mainly contributed by In 5s with a small amount of Tb 6s state

mixed in. For different Tb^{3+} ions concentrations, the In 5s state at lower conduction band decreased when Tb^{3+} ions doping concentration increased, causing CBM shift to higher energy level, and eventually increase in bandgap.

Having looked deep into the alloying nature of double perovskite NCs, we investigate the luminescence features. Under the excitation of 368 nm, Bi^{3+}-undoped $Cs_2AgInCl_6$ NCs showed blue emission at 470 nm instead of STEs emission and Bi^{3+}-doped $Cs_2AgInCl_6$ NCs showed broadband STEs emission at 580 nm, as reported before[35]. We also conduct the fs-TA spectroscopy for Bi^{3+}-doped $Cs_2AgInCl_6$ NCs to verify that the broadband orange emission originates from STEs. A broad photoinduced absorption upon excitation at 365 nm was observed as the direct character of self-trapped excitons (Figure S3).[39-41] As a comparison, as shown in Figure 4a, $Cs_2AgInCl_6$:20.6%Tb without Bi^{3+} ions exhibited no STEs emission and no characteristic luminescence of Tb^{3+} ions. The characteristic emission of Tb^{3+} ions could only be excited by its intrinsic excitation band at about 290 nm. However, after doping a small amount of Bi^{3+} ions, $Cs_2AgInCl_6$:20.6%Tb exhibited both broad emission derived from STEs and sharp emission peaks located at around 490 nm, 550 nm and 620 nm, corresponding to the intrinsic transition of Tb^{3+} ions $^5D_4$ - $^7F_6$, $^5D_4$ - $^7F_5$ and $^5D_4$ - $^7F_3$, respectively with the 368 nm excitation (Figure 4b). The excitation
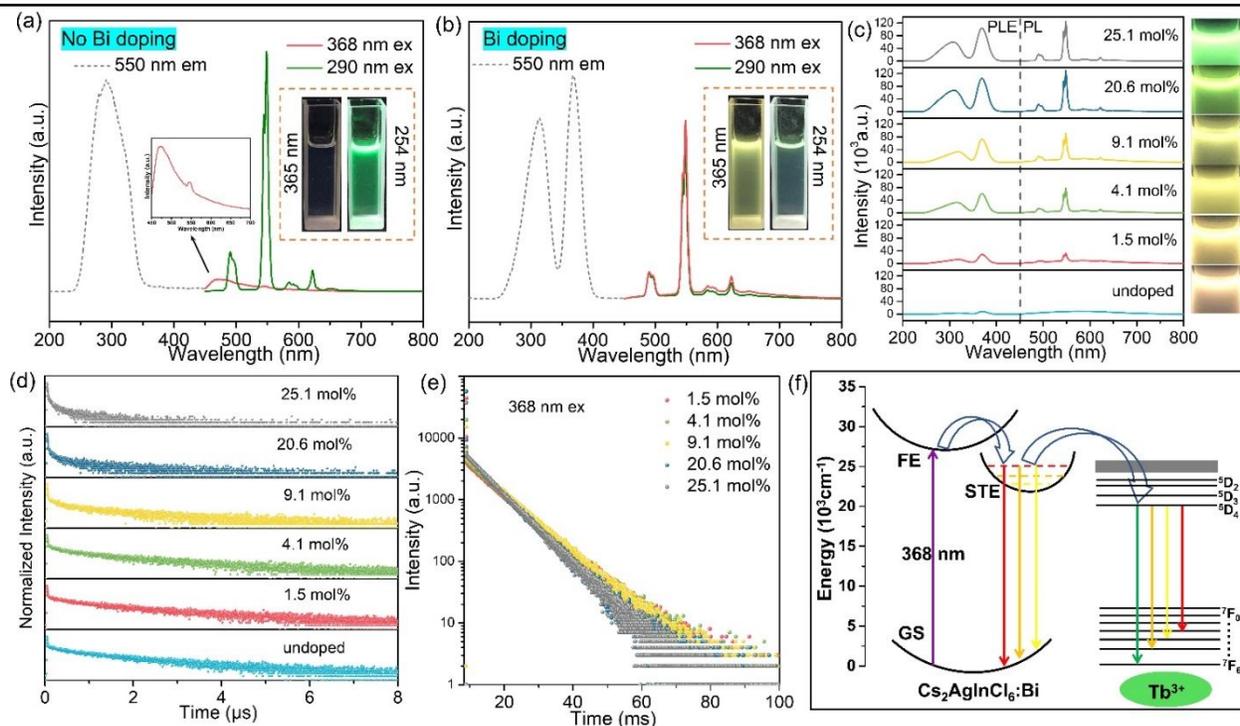
Figure 4. (a, b) Emission spectra (excited by 368 nm and 290 nm) and excitation spectra (monitored at 550 nm) of undoped (left) and Bi-doped $Cs_2AgInCl_6$:20.6%Tb (right), respectively. Insets show photographs of the corresponding sample under 254 nm and 365 nm UV irradiation. (c) PLE (left, monitored at 550 nm) and PL spectra (right, excited by 368 nm) of undoped and Tb^{3+}-doped $Cs_2AgInCl_6$:Bi NCs with different doping concentrations. Insets: the photos of the corresponding nanocrystals solution in hexane under the UV-light (365 nm) excitation. (d) PL decay curves of STEs emission from corresponding samples monitored at 368 nm excitation and 520 nm emission. (e) PL decay dynamics of Tb^{3+} ions emission (550 nm) from Tb^{3+}-doped $Cs_2AgInCl_6$:Bi NCs with different doping contents monitored at 368 nm excitation. (f) Energy level diagram of Tb^{3+} ions doped $Cs_2AgInCl_6$:Bi NCs and the proposed luminescence mechanism.

wavelength adjustment also endows the material with the wide range application. Indirectly, the phenomenon

suggested that the Tb^{3+} ions emission in $Cs_2AgInCl_6$:Bi,Tb NCs was not excited directly by 368 nm

but excited via an energy transfer channel from the $Cs_2AgInCl_6$:Bi,Tb NC host to Tb^{3+} ions. Moreover, the emission intensity excited by 368 nm was higher than that by 290 nm (Figure 4b), related to more efficient emission of Tb^{3+} ions through the energy transfer channel than directly via intrinsic excitation band, and the mechanism will be addressed below.

To shed more light on the doping concentration effect on luminescence properties of $Cs_2AgInCl_6$:Bi NCs, the controlled experiment for the samples with different amount of Tb^{3+} ions alloyed was conducted. As presented in Figure 4c and Figure S4, excited by 368 nm (the characteristic excitation of STEs in $Cs_2AgInCl_6$:Bi), the relative intensity of Tb^{3+} ions emission located at 550 nm increased gradually with incremental Tb^{3+} ions added and then decreased from 20.6 mol% Tb^{3+} ions alloyed caused by concentration quenching, which could be the direct existence of the energy transfer in the $Cs_2AgInCl_6$:Bi,Tb NCs from STEs to Tb^{3+} ions. Surprisingly, the STEs emission in highly Tb^{3+}-doped $Cs_2AgInCl_6$:Bi system almost disappeared and only the strong and sharp lines of Tb^{3+} ions emission existed, indicating that high doping concentration promoted the energy transfer from STEs to Tb^{3+} ions. Simultaneously, as a result of energy transfer, the concentration dependence of Tb^{3+} ions could further tune the emission colors of $Cs_2AgInCl_6$:Bi,Tb NCs from green to orange as shown in insets of Figure 4c. In addition, to further prove the existence of energy transfer channel, the photoluminescence decay curves for STEs emissions at different Tb^{3+} ions concentrations were measured and exhibited in Figure 4d. The monitored emission wavelength was 520 nm to avoid the interference of Tb^{3+} ions characteristic emission. The photoluminescence decay curves were fitted by triexponential functions with shorter-lived components (τ_1, τ_2 < 500 ns) possibly from deep surface trapping processes[42] and a longer-lived component (τ_3 > 500 ns) corresponding to the STEs lifetime (Table S5). It's known that the average lifetime (τ_{ave}) could be calculated by the following equation,[23]

$$\tau_{ave} = \sum_i A_i\tau_i$$

The values of average lifetimes (τ_{ave}) were calculated to be 1371.9, 1327.9, 1274.4, 993.7, 577.9, 319.5 ns corresponding to x = 0, 1.5, 4.1, 9.1, 20.6, 25.1 mol%, respectively. Thus, the lifetime for STEs decreased with the concentration of Tb^{3+} ions increased (Table S5), further indicating that the improved energy transfer from STEs to Tb^{3+} ions promoted the decay of STEs. The energy transfer efficiency η_T from STEs to Tb^{3+} ions can be obtained by the following calculation[43],

$$\eta_T = 1 - \tau_x/\tau_0$$

where τ_x and τ_0 are the lifetimes of STEs in the presence and absence of Tb^{3+} ions. The values of η_T were estimated to be 3.2%, 7.1%, 27.6%, 57.9% and 76.7% for x = 1.5, 4.1, 9.1, 20.6, 25.1 mol%, respectively, revealing that the energy transfer was efficient and the efficiency (η_T) increased with increase in Tb^{3+} ions concentration (Table S5). Besides, the PL decay curves of $Cs_2AgInCl_6$:Bi,Tb monitored at 550 nm were shown in Figure 4e. The

values of Tb^{3+} ions average lifetimes (τ_{ave}) were determined to be 8.9, 8.8, 8.7, 7.6, 7.4 ns at x = 1.5, 4.1, 9.1, 20.6, 25.1 mol%, respectively (Table S6). It is obvious that the lifetime of the Tb^{3+} ions decreases gradually as increase in Tb^{3+} ions content which can be ascribed to the concentration quenching effect. Based on the results discussed above, a possible photoluminescence mechanism for $Cs_2AgInCl_6$:Bi,Tb is proposed and shown in Figure 4f. Under the excitation at 368 nm, the electrons are excited from the ground states into the excited states of $Cs_2AgInCl_6$:Bi NC host and then shift to the self-trapped state through the nonradiative relaxation, emitting broad orange light due to the STEs recombination.[3,35] Simultaneously, partial energy is transferred to Tb^{3+} ion. Subsequently, electrons at higher level of Tb^{3+} ions are relaxed to the lowest excited level $^5D_4$, and then go back to the ground state, causing the Tb^{3+} ions ($^5D_4 \rightarrow {^7F_{6-3}}$) characteristic emission. And thus, the emission colors of $Cs_2AgInCl_6$:Bi,Tb NCs could be continuously tuned from green to orange.

CONCLUSION

In conclusion, we have reported the first example of Tb^{3+} ions incorporated $Cs_2AgInCl_6$:Bi NCs to impart and tune the photoluminescence. The structural analysis and the lowest formation energy of -4.77 eV for substitution doping of Tb^{3+} at In^{3+} site from first-principles calculation demonstrate the solid evidence that Tb^{3+} ions occupy In^{3+} sites in $Cs_2AgInCl_6$ NC hosts. Noted that Bi doping in $Cs_2AgInCl_6$ NCs adjust the excitation of Tb^{3+} ions and allow Tb^{3+} ions to exhibit the characteristic emission under 368 nm excitation, endowing the material with the potential light-emitting diode application with the excitation of commercial near ultraviolet chips. In addition, the introduction of Tb^{3+} ions brought tunable emission from green to orange and we have proposed the energy transfer channel with 368 nm excitation from STEs to Tb^{3+} ions in $Cs_2AgInCl_6$:Bi,Tb NCs. This work established the relationship between intrinsic emission from lead-free perovskite NCs and luminescence of lanthanide ions doping and further promoted the development of new lead-free perovskite NCs for emerging optoelectronic application.

ASSOCIATED CONTENT

Supporting Information. Fs TA spectra, structure refinement details, calculated bandgap details and fitted PL lifetimes of $Cs_2AgInCl_6$:Bi,Tb NCs. This material is available free of charge via the Internet at http://pubs.acs.org.

AUTHOR INFORMATION

Corresponding Author

* xiazg@scut.edu.cn (Z. Xia)

Author Contributions

6

‡These authors contributed equally.

REFERENCES

(1) Akkerman, Q. A.; Raino, G.; Kovalenko, M. V.; Manna, L., Genesis, Challenges and Opportunities for Colloidal Lead Halide Perovskite Nanocrystals. *Nat. Mater.* **2018,** *17*, 394-405.

(2) Huang, H.; Bodnarchuk, M. I.; Kershaw, S. V.; Kovalenko, M. V.; Rogach, A. L., Lead Halide Perovskite Nanocrystals in the Research Spotlight: Stability and Defect Tolerance. *ACS Energy Lett.* **2017,** *2*, 2071-2083.

(3) Luo, J.; Wang, X.; Li, S.; Liu, J.; Guo, Y.; Niu, G.; Yao, L.; Fu, Y.; Gao, L.; Dong, Q.; Zhao, C.; Leng, M.; Ma, F.; Liang, W.; Wang, L.; Jin, S.; Han, J.; Zhang, L.; Etheridge, J.; Wang, J.; Yan, Y.; Sargent, E. H.; Tang, J., Efficient and Stable Emission of Warm-white Light from Lead-free Halide Double Perovskites. *Nature* **2018,** *563*, 541-545.

(4) Ning, W.; Gao, F., Structural and Functional Diversity in Lead-Free Halide Perovskite Materials. *Adv. Mater.* **2019,** *31*, e1900326.

(5) Song, T.-B.; Yokoyama, T.; Aramaki, S.; Kanatzidis, M. G., Performance Enhancement of Lead-Free Tin-Based Perovskite Solar Cells with Reducing Atmosphere-Assisted Dispersible Additive. *ACS Energy Lett.* **2017,** *2*, 897-903.

(6) Igbari, F.; Wang, Z. K.; Liao, L. S., Progress of Lead-Free Halide Double Perovskites. *Adv. Energy Mater.* **2019,** *9*, 1803150.

(7) Cai, Y.; Xie, W.; Teng, Y. T.; Harikesh, P. C.; Ghosh, B.; Huck, P.; Persson, K. A.; Mathews, N.; Mhaisalkar, S. G.; Sherburne, M.; Asta, M., High-throughput Computational Study of Halide Double Perovskite Inorganic Compounds. *Chem. Mater.* **2019,** *31*, 5392-5401.

(8) Locardi, F.; Cirignano, M.; Baranov, D.; Dang, Z.; Prato, M.; Drago, F.; Ferretti, M.; Pinchetti, V.; Fanciulli, M.; Brovelli, S.; De Trizio, L.; Manna, L., Colloidal Synthesis of Double Perovskite $Cs_2AgInCl_6$ and Mn-Doped $Cs_2AgInCl_6$ Nanocrystals. *J. Am. Chem. Soc.* **2018,** *140*, 12989-12995.

(9) Yang, B.; Mao, X.; Hong, F.; Meng, W.; Tang, Y.; Xia, X.; Yang, S.; Deng, W.; Han, K., Lead-Free Direct Band Gap Double-Perovskite Nanocrystals with Bright Dual-Color Emission. *J. Am. Chem. Soc.* **2018,** *140*, 17001-17006.

(10) Bekenstein, Y.; Dahl, J. C.; Huang, J.; Osowiecki, W. T.; Swabeck, J. K.; Chan, E. M.; Yang, P.; Alivisatos, A. P., The Making and Breaking of Lead-Free Double Perovskite Nanocrystals of Cesium Silver-Bismuth Halide Compositions. *Nano Lett.* **2018,** *18*, 3502-3508.

(11) Yang, B.; Hong, F.; Chen, J.; Tang, Y.; Yang, L.; Sang, Y.; Xia, X.; Guo, J.; He, H.; Yang, S.; Deng, W.; Han, K., Colloidal Synthesis and Charge-Carrier Dynamics of $Cs_2AgSb_{1-y}Bi_yX_6$ (X: Br, Cl; $0 \le y \le 1$) Double Perovskite Nanocrystals. *Angew. Chem. Int. Ed.* **2019,** *58*, 2278-2283.

(12) Du, K. Z.; Meng, W.; Wang, X.; Yan, Y.; Mitzi, D. B., Bandgap Engineering of Lead-Free Double Perovskite $Cs_2AgBiBr_6$ through Trivalent Metal Alloying. *Angew. Chem. Int. Ed.* **2017,** *56*, 8158-8162.

(13) Karmakar, A.; Dodd, M. S.; Agnihotri, S.; Ravera, E.; Michaelis, V. K., Cu(II)-Doped $Cs_2SbAgCl_6$ Double Perovskite: A Lead-Free, Low-Bandgap Material. *Chem. Mater.* **2018,** *30*, 8280-8290.

(14) Meng, W.; Wang, X.; Xiao, Z.; Wang, J.; Mitzi, D. B.; Yan, Y., Parity-Forbidden Transitions and Their Impact on the Optical Absorption Properties of Lead-Free Metal Halide Perovskites and Double Perovskites. *J. Phys. Chem. Lett.* **2017,** *8*, 2999-3007.

(15) Lamba, R. S.; Basera, P.; Bhattacharya, S.; Sapra, S., Band Gap Engineering in $Cs_2(Na_xAg_{1-x})BiCl_6$ Double Perovskite Nanocrystals. *J. Phys. Chem. Lett.* **2019,** *10*, 5173-5181.

(16) Zhou, J.; Rong, X.; Zhang, P.; Molokeev, M. S.; Wei, P.; Liu, Q.; Zhang, X.; Xia, Z., Manipulation of Bi^{3+}/In^{3+} Transmutation and Mn^{2+}-Doping Effect on the Structure and Optical Properties of Double Perovskite $Cs_2NaBi_{1-x}In_xCl_6$. *Adv. Opt. Mater.* **2019,** *7*, 1801435.

(17) Mir, W. J.; Sheikh, T.; Arfin, H.; Xia, Z.; Nag, A., Lanthanide Doping in Metal Halide Perovskite Nanocrystals: Spectral Shifting, Quantum Cutting and Optoelectronic Applications. *NPG Asia Materials* **2020,** *12*, 9.

(18) Pan, G.; Bai, X.; Yang, D.; Chen, X.; Jing, P.; Qu, S.; Zhang, L.; Zhou, D.; Zhu, J.; Xu, W.; Dong, B.; Song, H., Doping Lanthanide into Perovskite Nanocrystals: Highly Improved and Expanded Optical Properties. *Nano Lett.* **2017,** *17*, 8005-8011.

(19) Kroupa, D. M.; Roh, J. Y.; Milstein, T. J.; Creutz, S., E.,; Gamelin, D., R., Quantum-Cutting Ytterbium-Doped $CsPb(Cl_{1-x}Br_x)_3$ Perovskite Thin Films with Photoluminescence Quantum Yields over 190%. *ACS Energy Lett.* **2018,** *3*, 2390-2395.

(20) Zhou, D.; Liu, D.; Pan, G.; Chen, X.; Li, D.; Xu, W.; Bai, X.; Song, H., Cerium and Ytterbium Codoped Halide Perovskite Quantum Dots: A Novel and Efficient Downconverter for Improving the Performance of Silicon Solar Cells. *Adv. Mater.* **2017,** *29*, 1704149.

(21) Mir, W. J.; Mahor, Y.; Lohar, A.; Jagadeeswararao, M.; Das, S.; Mahamuni, S.; Nag, A., Postsynthesis Doping of Mn and Yb into $CsPbX_3$ (X = Cl, Br, or I) Perovskite Nanocrystals for Downconversion Emission. *Chem. Mater.* **2018,** *30*, 8170-8178.

(22) Yao, J. S.; Ge, J.; Han, B. N.; Wang, K. H.; Yao, H. B.; Yu, H. L.; Li, J. H.; Zhu, B. S.; Song, J. Z.; Chen, C.; Zhang, Q.; Zeng, H. B.; Luo, Y.; Yu, S. H., Ce^{3+}-Doping to Modulate Photoluminescence Kinetics for Efficient $CsPbBr_3$ Nanocrystals Based Light-Emitting Diodes. *J. Am. Chem. Soc.* **2018,** *140*, 3626-3634.

(23) Luo, C.; Li, W.; Fu, J.; Yang, W., Constructing Gradient Energy Levels to Promote Exciton Energy Transfer for Photoluminescence Controllability of All-Inorganic Perovskites and Application in Single-Component WLEDs. *Chem. Mater.* **2019,** *31*, 5616-5624.

(24) Lee, W.; Hong, S.; Kim, S., Colloidal Synthesis of Lead-Free Silver–Indium Double-Perovskite $Cs_2AgInCl_6$ Nanocrystals and Their Doping with Lanthanide Ions. *J. Phys. Chem. C* **2019,** *123*, 2665-2672.

(25) Mahor, Y.; Mir, W. J.; Nag, A., Synthesis and Near-Infrared Emission of Yb-Doped $Cs_2AgInCl_6$ Double Perovskite Microcrystals and Nanocrystals. *J. Phys. Chem. C* **2019,** *123*, 15787-15793.

(26) Chen, N.; Cai, T.; Li, W.; Hills-Kimball, K.; Yang, H.; Que, M.; Nagaoka, Y.; Liu, Z.; Yang, D.; Dong, A.; Xu, C. Y.; Zia, R.; Chen, O., Yb- and Mn- Doped Lead-Free Double Perovskite Cs_2AgBiX_6 (X = Cl^-, Br^-) Nanocrystals. *ACS Appl. Mater. Interfaces* **2019,** *11*, 16855-16863.

(27) Li, S.; Hu, Q.; Luo, J.; Jin, T.; Liu, J.; Li, J.; Tan, Z.; Han, Y.; Zheng, Z.; Zhai, T.; Song, H.; Gao, L.; Niu, G.; Tang, J., Self-Trapped Exciton to Dopant Energy Transfer in Rare Earth Doped Lead-Free Double Perovskite. *Adv. Opt. Mater.* **2019,** *7*, 1901098.

7

(28) Ding, N.; Zhou, D.; Pan, G.; Xu, W.; Chen, X.; Li, D.; Zhang, X.; Zhu, J.; Ji, Y.; Song, H., Europium-Doped Lead-Free $Cs_3Bi_2Br_9$ Perovskite Quantum Dots and Ultrasensitive Cu^{2+} Detection. *ACS Sustainable Chem. Eng.* **2019,** *7*, 8397-8404.

(29) Kresse, G.; Furthmuller, J., Efficiency of Ab-initio Total Energy Calculations for Metals and Semiconductors Using a Plane-wave Basis Set. *Comput. Mater. Sci.* **1996,** *6*, 15-50.

(30) Kresse, G.; Furthmuller, J., Efficient Iterative Schemes for Ab Initio Total-energy Calculations Using a Plane-wave Basis Set. *Phys. Rev. B* **1996,** *54*, 11169-11186.

(31) Blochl, P. E., Projector Augmented-wave Method. *Phys. Rev. B* **1994,** *50*, 17953-17979.

(32) Perdew, J. P.; Burke, K.; Ernzerhof, M., Generalized Gradient Approximation Made Simple. *Phys. Rev. Lett.* **1996,** *77*, 3865-3868.

(33) Monkhorst, H. J.; Pack, J. D., Special Points for Brillouin-zone Integrations. *Phys. Rev. B* **1976,** *13*, 5188-5192.

(34) Zhou, J.; Rong, X.; Molokeev, M. S.; Zhang, X.; Xia, Z., Exploring the Transposition Effects on the Electronic and Optical Properties of $Cs_2AgSbCl_6$ via a Combined Computational-Experimental Approach. *J. Mater. Chem. A* **2018,** *6*, 2346-2352.

(35) Liu, Y.; Jing, Y.; Zhao, J.; Liu, Q.; Xia, Z., Design Optimization of Lead-Free Perovskite $Cs_2AgInCl_6$:Bi Nanocrystals with 11.4% Photoluminescence Quantum Yield. *Chem. Mater.* **2019,** *31*, 3333-3339.

(36) Zhou, J.; Xia, Z.; Molokeev, M. S.; Zhang, X.; Peng, D.; Liu, Q., Composition Design, Optical Gap and Stability Investigations of Lead-free Halide Double Perovskite $Cs_2AgInCl_6$. *J. Mater. Chem. A* **2017,** *5*, 15031-15037.

(37) Ma, J.-P.; Chen, Y.-M.; Zhang, L.-M.; Guo, S.-Q.; Liu, J.-D.; Li, H.; Ye, B.-J.; Li, Z.-Y.; Zhou, Y.; Zhang, B.-B.; Bakr, O. M.; Zhang, J.-Y.; Sun, H.-T., Insights into the Local Structure of Dopants, Doping efficiency, and Luminescence Properties of Lanthanide-doped $CsPbCl_3$ Perovskite Nanocrystals. *J. Mater. Chem. C* **2019,** *7*, 3037-3048.

(38) Zhou, J.; Luo, J.; Rong, X.; Wei, P.; Molokeev, M. S.; Huang, Y.; Zhao, J.; Liu, Q.; Zhang, X.; Tang, J.; Xia, Z., Lead-Free Perovskite Derivative $Cs_2SnCl_{6-x}Br_x$ Single Crystals for Narrowband Photodetectors. *Adv. Opt. Mater.* **2019,** *7*, 1900139.

(39) Li, M.; Zhou, J.; Zhou, G.; Molokeev, M. S.; Zhao, J.; Morad, V.; Kovalenko, M. V.; Xia, Z., Hybrid Metal Halides with Multiple Photoluminescence Centers. *Angew. Chem. Int. Ed.* **2019,** *58*, 18670-18675.

(40) Zhang, R.; Mao, X.; Yang, Y.; Yang, S.; Zhao, W.; Wumaier, T.; Wei, D.; Deng, W.; Han, K., Air-Stable, Lead-Free Zero-Dimensional Mixed Bismuth-Antimony Perovskite Single Crystals with Ultra-broadband Emission. *Angew. Chem. Int. Ed.* **2019,** *58*, 2725-2729.

(41) Zhou, L.; Liao, J. F.; Huang, Z. G.; Wei, J. H.; Wang, X. D.; Chen, H. Y.; Kuang, D. B., Intrinsic Self-Trapped Emission in 0D Lead-Free $(C_4H_{14}N_2)_2In_2Br_{10}$ Single Crystal. *Angew. Chem. Int. Ed.* **2019,** *58*, 15435-15440.

(42) Slavney, A. H.; Hu, T.; Lindenberg, A. M.; Karunadasa, H. I., A Bismuth-Halide Double Perovskite with Long Carrier Recombination Lifetime for Photovoltaic Applications. *J. Am. Chem. Soc.* **2016,** *138*, 2138-2141.

(43) Zhou, J.; Xia, Z., Multi-color Emission Evolution and Energy Transfer Behavior of $La_3GaGe_5O_{16}$:Tb^{3+},Eu^{3+} Phosphors. *J. Mater. Chem. C* **2014,** *2*, 6978-6984.